ELSEVIER

Contents lists available at ScienceDirect

Materialia

journal homepage: www.elsevier.com/locate/mtla

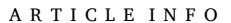


Full Length Article

Carbonate environment changes with Na or K substitution in biomimetic apatites

Stephanie L. Wong a,b, Christophe Drouet b, Alix Deymier a,*

- a Department of Biomedical Engineering, UConn Health Center, Farmington, CT, USA
- b CIRIMAT, CNRS, University of Toulouse, Toulouse, France



Keywords:
Biomimetic apatite
Sodium
Potassium
Carbonate
FTIR

ABSTRACT

Biological and biomimetic apatites allow incorporations of many cationic and anionic substituents, namely Na⁺, CO₃²⁻, and potentially K⁺, that influence apatite's physicochemical, thermodynamic, and structural properties. Carbonate substitution can modify these properties depending on the CO₃⁻ type, such as hydroxyl (A-type) or phosphate (B-type) sites, or labile ions within the non-apatitic surface layer. While Na⁺ co-substitutions can affect CO_3^{2-} integration, it is unknown if and how K^+ , a larger cation, may affect CO_3^{2-} substitution and related apatite properties. Therefore, the purpose of this study was to compare the effects of K⁺ and Na⁺ on the physicochemical incorporation of CO_3^{2-} in biomimetic apatites. To do so, 2-6 wt% CO_3^{2-} apatites were precipitated in either Na- or K-rich solutions under optimized synthesis and maturation conditions. Atomic absorption data showed more Na⁺ substitution into the apatite structure than K⁺. FTIR and XRD results indicated that Na-apatites primarily contained B-type CO_3^{2-} , while K-apatites included more A-type CO_3^{2-} at higher total wt% CO_3^{2-} . A deep FTIR analysis of the CO_3^2 vibration modes showed that a red-shift occurred for the $\nu_2 CO_3^2$ and $\nu_3 CO_3^2$ B-type of the Na-apatites, suggesting a longer C—O bond length, while K-apatites had a slight blue-shift for only $\nu_2 \text{CO}_3^2$. Apatitic and non-apatitic HPO₄²⁻ retention was also higher for Na-apatites than K-apatites. Together, these observations suggest that modification of the local CO_3^{2-} environments depends on the monovalent cation. Overall, our data reveals the distinct mechanisms for Na⁺/CO₃²⁻ and K⁺/CO₃²⁻ co-substitution, which may shed light on the carbonation of biological apatites and their structural features.

1. Introduction

The inorganic component of bone and dentin is composed of carbonate-substituted apatite nanocrystals with a nonstoichiometric apatitic core covered by an amorphous hydrated layer bearing labile ions [1–4]. The surrounding body fluids that envelop these biominerals undergo constant changes related to the time of day, nutrition, aging, homeostatic equilibrations, etc. [5–8]. In turn, these changes can allow dissolution and recrystallization phenomena on a regular basis, allowing for ionic substitutions within the apatite crystal lattice [9–12]. In this view, bone and teeth minerals are far from an inert component and should be seen as a dynamic reservoir for ionic species. The cationic and anionic substitutions that apatite allows can then impact many chemical, physical, and structural properties of the apatite mineral [13–16]. Synthesizing biomimetic apatites by utilizing close-to-physiological methodologies provides the same main characteristics of biological

apatite – namely nanosized crystal dimensions, nonstoichiometry, and a hydrated ionic surface layer on the nanocrystals. Like biological apatite (except mature tooth enamel), biomimetic analogs are nonstoichiometric and often accommodate substituting ions, that modulate thermodynamic properties [17,18].

Among common ionic substitutions in biologically relevant apatites are carbonate (CO_3^{2-}) ions. Naturally, bone mineral has CO_3^{2-} incorporation ranging from 2 to 6 wt% depending on the location, tissue type, and local bone aging where newly-formed bone apatite has relatively low CO_3^{2-} content that increases with aging [19,20]. In the apatite structure, CO_3^{2-} ions can replace either the OH⁻ ions in the apatitic channel (A-type CO_3^{2-}) or phosphate (PO_4^{3-}) ions (B-type CO_3^{2-}) (Fig. 1) [21]. Carbonate can also reside in the hydrated surface layer of nanocrystalline apatites, known as the labile CO_3^{2-} species (Fig. 1) [22,23]. Due to changes in molecular geometry and size between the CO_3^{2-} , PO_4^{3-} , and OH^- ions, the crystal unit cell parameters of the a-axis and c-axis can

E-mail address: deymier@uchc.edu (A. Deymier).



^{*} Corresponding author: UCH-Dept. of Biomedical Engineering, University of Connecticut School of Dental Medicine, 263 Farmington Avenue, Mail Code: 1721, Farmington, CT, 06030.

increase upon increasing A-type or B-type CO_3^2 -substitution, respectively [24]. Besides structural modifications, B-type CO_3^2 increases the solubility and decreases the stiffness and surface energy of the apatite [13], while A-type CO_3^2 substitution was reported to change surface water absorption and is thermodynamically more stable at higher temperatures [25,26].

Along with CO_3^{2-} substitution, several other ions can also substitute for calcium (Ca^{2+}), PO_4^{3-} or OH^- , at least to some extent. The readiness to substitute a given ion appears to be a complex process dependent on several factors. Not only the ionic size and charge seem to influence the (de)stabilization of the apatitic lattice, but also some intrinsic physical features of the elements themselves, such as their Pauling electronegativity [18]. Among monovalent cations, sodium (Na⁺) ions were found to integrate into the apatite lattice to a notable extent [27]. This may occur in vivo, taking into account the large sodium concentration in body fluids (e.g. 145 mM in blood compared to 1.8 mM for calcium) and leading to an average of 1.0 wt% Na⁺ in (bovine) cortical bone [28,29]. This integration also occurs synthetically in the presence of Na⁺. In both instances, Na⁺ may have an affinity to incorporate into the apatite structure. While Na⁺ ionic radius is somewhat larger than Ca²⁺, but smaller than other cations, such as potassium (K⁺), sodium's electronegativity is fairly close to Ca²⁺ (Table 1). It is unclear whether Na⁺ ions may also reside in the hydrated layer of the nanocrystals or solely in the apatitic core. However, recent findings suggest that both options may be possible [30,31]. Previous studies have observed the important role of Na⁺ on apatite and CO₃²⁻ incorporation, such as promoting the overall uptake of CO_3^{2-} into a patite and increasing the amount of both ions [32, 33]. To balance the crystal charge, Na⁺ is optimally co-substituted into the Ca^{2+} sites when PO_4^{3-} is replaced by CO_3^{2-} , promoting B-type CO_3^{2-} [12,34]. Additionally, the incorporation of Na⁺ can alter the vibrational signature of CO₃²⁻ ions, indicating that Na⁺ changes the spatial configurations of CO_3^{2-} within apatite [27,33]. However, many of these results originated from apatite samples prepared at high pressure and/or

Table 1Effective ionic radii for Ca²⁺, Na⁺ and K⁺ for coordination VI, VII and IX [35] and their Pauling electronegativity [36].

Coordination Number	Ca ²⁺	Na ⁺	K ⁺
VI	1.00	1.02	1.38
VII (Call sites in apatite)	1.07	1.13	1.46
IX (Cal sites in apatite)	1.18	1.32	1.55
Pauling electronegativity	Ca	Na	K
χ	1.00	0.93	0.82

temperature, which is potentially distant from biological apatites, or their biomimetic counterparts formed at relatively low temperatures.

In addition to Na+, other transition and alkali-earth metal elements can also easily incorporate into the apatite lattice, such as Mg, Ti, Fe, Mn, Cu, Ag and Zn [37]. Their properties on apatite have been studied extensively and have also been compared to Na⁺[37]. Conversely, the incorporation of K⁺ has been considerably less documented. Yet, about 0.07 wt% K⁺ is present in average (bovine) cortical bone [29]. Its significantly larger ionic size (Table 1) may potentially hinder its integration into the apatite lattice, resulting in substantially less K⁺ and CO_3^{2-} incorporation compared to Na⁺ and CO_3^{2-} [15]. While there are several studies probing the effect of Na⁺ on CO₃²⁻ incorporation [30,32, 33,38–42], there is even less information about the relationship between K^+ and CO_3^2 in biomimetic apatites [15,40,43,44]. In addition, it is unclear if different mechanisms are linked to CO_3^{2-} incorporation. Therefore, we set out to understand how K⁺ and Na⁺ substitution affects the chemical and physical incorporation of CO_3^{2-} in biomimetic apatite. Understanding the mechanism of Na⁺ and K⁺ co-substitutions with CO₃²⁻ can elucidate how the physicochemical properties of biological apatite may change with body fluid composition, including pathological and pharmacological Na⁺ or K⁺ influxes. In addition, manipulating CO_3^{2-} types, concentration, and substitution mechanisms may benefit future setups in the development of resorbable bone substitutes.

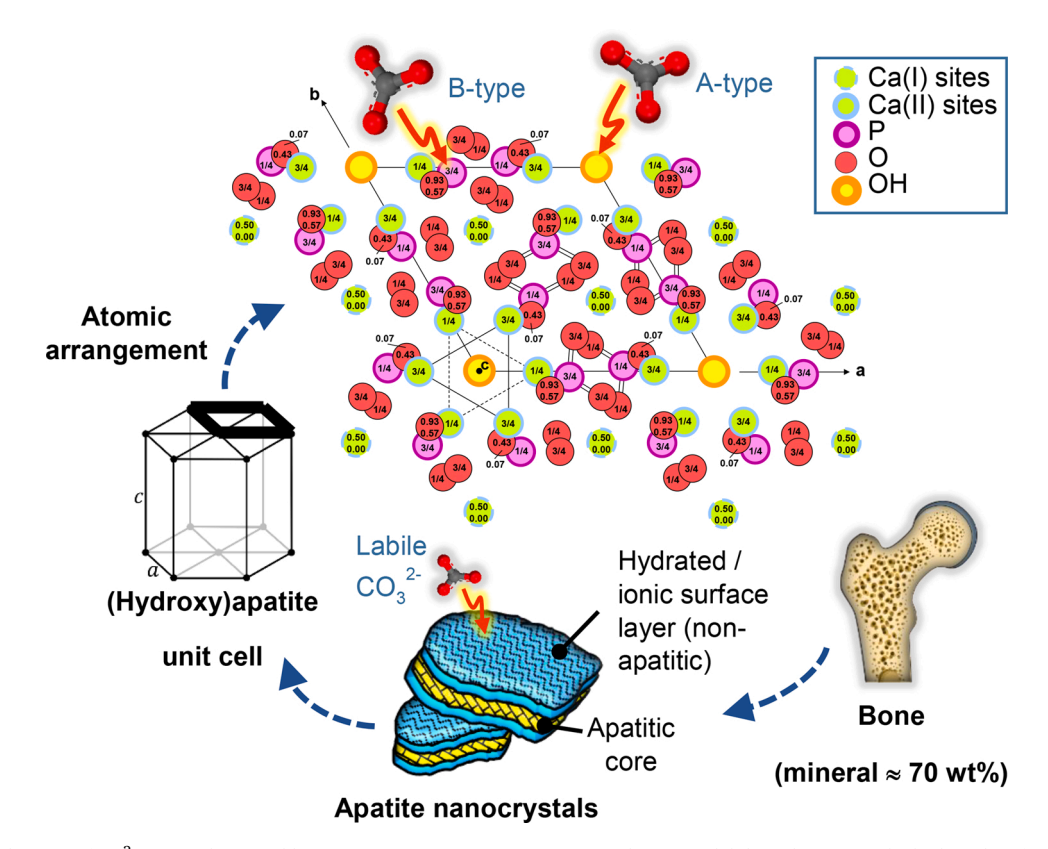


Fig. 1. Possible localization of CO_3^{2-} ions in bone and biomimetic apatites. Apatite nanocrystals contain labile carbonate on the hydrated surface layer of the crystal. Within the apatite unit cell, carbonate can also substitute for the PO_3^{4-} or OH^- groups, known as B-type or A-type CO_3^{2-} , respectively.

2. Materials and methods

2.1. Synthesis

Nanocrystalline apatite samples with controlled carbonate contents of 2, 4, or 6 wt% were synthesized by precipitation in either Na-rich or K-rich environments using similar aqueous methods as previously described [45]. Briefly, for the Na-rich environments, 0.295 M of calcium nitrate tetrahydrate (Ca(NO₃)₂•4H₂O, Sigma Life Science) was poured into a solution with a 1:1 CO_3^{2-}/PO_4^{3-} molar ratio of 0.91 M of diammonium hydrogen phosphate ((NH₄)₂HPO₄, Carlo Erba reagents) and 1.43 M sodium bicarbonate (NaHCO₃, VWR Normapur Prolabo). For the K-rich environments, a 1:1 or 2:1 molar ratio of CO_3^{2-}/PO_4^{3-} was used with potassium bicarbonate (KHCO3, Rectapur Prolabo) depending on the aimed carbonate content. These precipitating conditions allowed for an excess of phosphate ions to provide inherent buffering of the solution without the addition of external agents, such as tris(hydroxymethyl) aminomethane (TRIS), and to favor bone-like apatite crystallization to occur. To further mimic maturing bone mineral, the precipitates were matured for either 20 min, 1 day, or 3 days at room temperature or 60 °C (Table 2) to attain increasingly matured apatite samples and to obtain CO₃-ranges similar to bone. Afterwards, the powders were filtered, thoroughly rinsed with deionized water, and lyophilized.

2.2. Atomic absorption spectroscopy (AAS)

To analyze the calcium, sodium, and potassium contents, 100 mg of each apatite sample was dissolved in 1% (v/v) of 69% nitric acid (HNO $_3$, VWR) to prepare 1 mg/mL stock solutions. The solutions were further diluted with 1% (v/v) of 69% nitric acid, 0.5% (v/v) of La(NO $_3$)3 (SCP Science – 140-003-451), and 0.5% (v/v) of CsCl (SCP Science – 140-003-241) according to the element calibration range measured by the Thermo Scientific iCE 3000 Series Atomic Absorption spectrometer. The instrument was calibrated with elemental standards and controls before data acquisition (R 2 = 0.9951). Blanks and standards were regularly measured after every 5 samples to verify accuracy and absence of deviations. Stoichiometric hydroxyapatite was also used as a control sample.

2.3. Fourier transform infrared spectroscopy (FTIR)

Transmission FTIR using a Nicolet 5700 spectrometer and the OMNIC 8 software (Thermo Nicolet) were used to confirm and analyze the characteristics of the bone-like apatite phases as well as the composition, specifically for the apatitic and non-apatitic $\text{CO}_3^{2^-}$ and $\text{HPO}_4^{2^-}$ groups. Each apatite specimen was mixed and crushed with KBr (Uvasol) to make pellets with an absorbance of ~1.0 for the highest peak of the ν_3 PO₄ vibration mode, using an acquisition of 64 scans with 4 cm⁻¹ resolution (400–4000 cm⁻¹). The ν_4 PO₄, ν_3 CO₃ and $\nu_1\nu_3$ PO₄ vibration modes were particularly scrutinized. The total carbonate content of the apatites was calculated by obtaining the area ratio of the (ν_3 CO₃/ $\nu_1\nu_3$ PO₄) bands and using the linear fit, wt% CO₃² = 28.62 × (CO₃/PO₄) + 0.0843, as previously quantified and validated by Grunenwald et al. [46].

Additional "concentrated" apatite/KBr pellets were made to acquire

Table 2Synthesis conditions used for each biomimetic apatite.

Na vs K	~2%	~4%	~6%
Na	1:1 CO ₃ /PO ₄ Maturation 20 min, RT	1:1 CO ₃ /PO ₄ Maturation 3 days, RT	1:1 CO ₃ /PO ₄ Maturation 1 day, 60 °C
K	1:1 CO ₃ /PO ₄ Maturation 3 days, RT	1:1 CO ₃ /PO ₄ Maturation 1 day, 60 °C	2:1 CO ₃ /PO ₄ Maturation 1 day, 60 °C

an absorbance of >2.0 (for the highest peak of ν_3 PO₄) using an acquisition of 64 scans and a greater resolution of 2 cm⁻¹, to better resolve the ν_2 CO₃, ν_2 PO₄, and ν_4 PO₄ vibration domains. Using a Lorentzian fit function in OriginPro 2021b (OriginLab Corporation, Northampton, MA, USA), the peaks in the 750–400 cm⁻¹ range were deconvoluted (Fig. 2a) for the ν_2 PO₄ (~470 cm⁻¹), non-apatitic HPO₄ (534 cm⁻¹), apatitic HPO₄ (550 cm⁻¹), apatitic PO₄ (660, 575, and 603 cm⁻¹), non-apatitic PO₄ (617 cm⁻¹), apatitic OH (631 cm⁻¹), and H₂O (~685 cm⁻¹). The total combined area of non-apatitic and apatitic HPO₄² was used in the deconvolution of the ν_2 CO₃ peak as described previously [47] to subtract the HPO₄² contribution in this spectral domain. The standard deviation was calculated by propagating the fitting errors.

For the out-of-plane ν_2 CO $_3$ deformation mode, initial positions for the fitting parameters were A-type CO_3^2 (880 cm⁻¹), B-type (873 cm⁻¹) and labile CO_3^2 (864 cm⁻¹). Since HPO₄²⁻ ions are highly present in bone and biomimetic apatites and exhibit a notable band in the same spectral range (at \sim 870 cm⁻¹), this band was also included in the analysis (Fig. 2b). While the B-type CO_3^{2-} contribution used a Lorentzian fitting function, all other constitutive contributions in this spectral domain were fitted using a Gaussian function due to the broad peak distributions. The peak wavenumbers and area were then calculated. To obtain the wt% of each CO_3^{2-} type, each CO_3^{2-} contribution was normalized by the total area of all CO_3^{2-} types within the ν_2 CO_3 domain. Afterwards, the normalized area of each type of carbonate was divided by the total wt% CO_3^{2-} of the apatite determined previously by the area ratio of the $(\nu_3 \text{CO}_3/\nu_1\nu_3 \text{PO}_4)$ [47]. The standard deviation was calculated by averaging the triplicate fitting analyses of each sample within OriginPro 2021b. In addition to the ν_2 CO₃, the ν_3 CO₃ asymmetric stretching mode was also examined. Fourier self-deconvolution (apodization) was performed to further highlight the underlying superimposed band positions for each CO_3^{2-} type, using the corresponding built-in processing tool of the OMNIC 8 software (Thermo Nicolet) with a typical bandwidth of 20.4 cm⁻¹ and an enhancement factor of 1.4.

In general, the type of CO_3^{2-} species (A-, B-, or labile/surface types) was determined by analyzing the ν_2 CO₃ out-of-plane deformation mode because this vibration mode provides a single peak for any given chemical environment, i.e. generating one single peak per CO_3^{2-} type. The ν_3 CO₃ asymmetric stretching mode leads to a doublet peak for every CO_3^{2-} type, thus generating a complex band formed by highly overlapped spectral contributions. The singlet versus doublet characters of the ν_2 CO₃ and ν_3 CO₃ modes respectively (for each CO₃²⁻ type) arise from two things: (1) The symmetry of the free CO_3^{2-} ion related to the D_{3h} point symmetry (leading to the non-degenerate irreducible representation A''_2 for ν_2 CO₃ and to the doubly-degenerate irreducible representation E' for ν_3 CO₃) and (2) the splitting of the initially degenerate v_3 CO₃ mode due to the lowered symmetry at the crystal site [48]. The crystal electrostatic field generated by the nearest neighbors of the CO_3^2 ion indeed affects the vibrational energy levels. In this regard, it is more accurate to determine the relative amounts of each CO_3^{2-} type from the analysis of the ν_2 CO₃ mode compared to the ν_3 CO₃ mode, as was also highlighted elsewhere [27].

2.4. X-ray diffraction (XRD)

XRD was used to confirm the apatite crystallographic features, and patterns were especially analyzed for (002) and (310) lattice spacing, crystallinity, and crystallite length and width. Using a Bruker D8 Advance XRD system operating at 40 kV and 40 mA ($\lambda_{k\alpha}=1.5418~\mathring{A}$), the patterns were recorded within the range $2\theta=20^\circ-80^\circ$ with a step of 0.02° and 3 second acquisition time per step. The peak centers and the Full Width at Half Maximum (FWHM) for the (002) and (310) were analyzed and peak fitted, using a PseudoVoigt function with the Diffrac. eva software. The powder patterns were compared to stoichiometric hydroxyapatite (PDF 09-0432) from the Powder Diffraction File open database from the International center for Diffraction Data (ICDD). The crystallite length and width were determined by Scherrer's equation

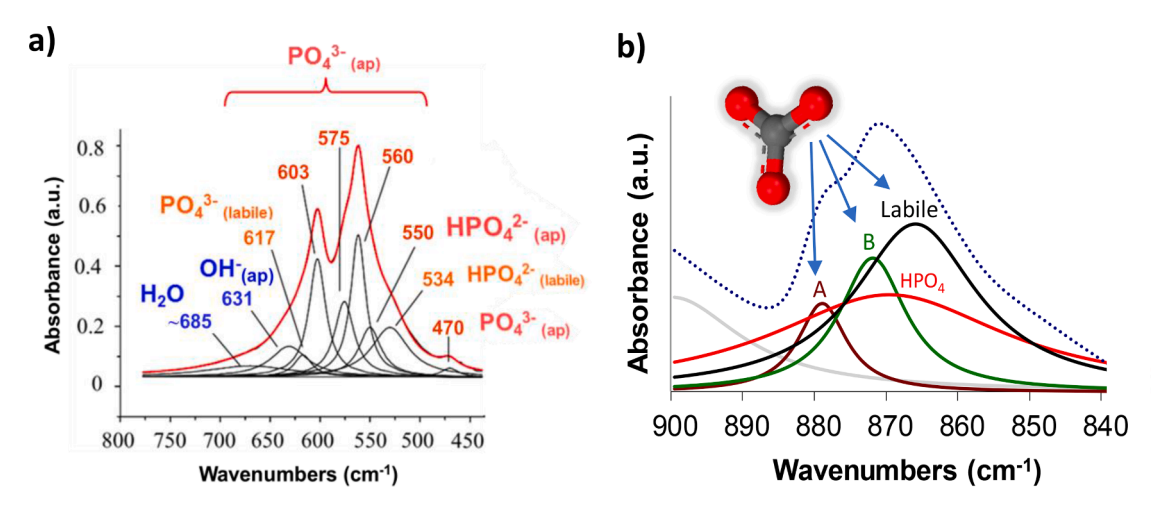


Fig. 2. FTIR deconvolutions. (a) The initial peak deconvolution parameters used for the ν_4 PO₄ vibration mode. The combined areas of the apatitic and labile HPO₄²⁻ were used in the (b) initial ν_2 CO₃²⁻ peak deconvolution.

using the FWHM.

3. Results

3.1. Sample synthesis

To investigate the effect of Na^+ and K^+ on carbonate incorporation in nanocrystalline apatites, apatite samples were prepared with targeted carbonate contents of 2, 4, or 6 wt% relevant to the bone compositional domain. The main physicochemical characteristics of the obtained samples were analyzed by several complementary techniques as indicated below.

3.2. Atomic absorption spectroscopy (AAS)

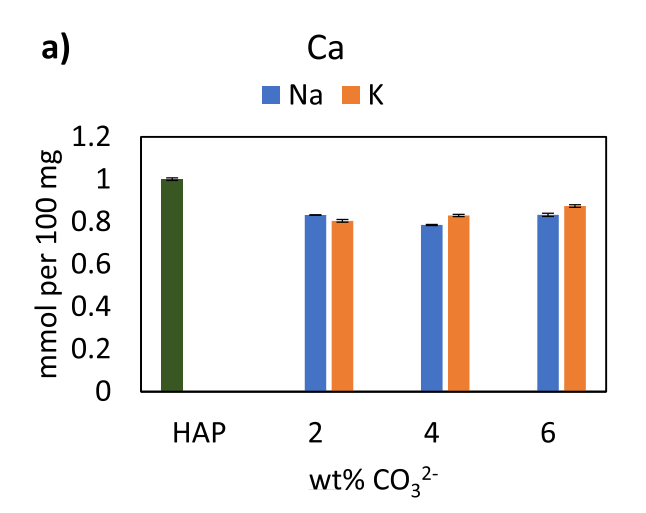
The calcium content within each apatite was measured for 100 mg of sample. For Na-apatites, the amount of calcium for the samples with 2, 4, and 6 wt% $\rm CO_3^2$ was 0.83, 0.78, 0.83 mmol, respectively (Fig. 3a). For K-apatites, calcium steadily increased as the carbonate content increased (0.80, 0.83, and 0.87 mmol, respectively). In both cases, the calcium values remained lower than stoichiometric hydroxyapatite (1.00 mmol). Sodium and potassium contents were similarly determined for 100 mg of sample. The sodium concentration increased (0.0063, 0.023, 0.079 mmol) by a factor \sim 3.5 × for each doubling of carbonate

content. The potassium content was detected at significantly lower amounts with increasing potassium as carbonate increased (6.46 \times $10^{-4},~1.86\times~10^{-3},~3.17\times~10^{-3}$ mmol for 2, 4, and 6 wt% CO_3^{2-} , respectively).

3.3. FTIR spectroscopy

For all samples, FTIR analyses showed the characteristic vibration bands of bone-like apatite (Sup. Fig. 1a–c). Using previously established methods [46], the degree of carbonate incorporation was analyzed by the peak area ratio of the ν_3 CO $_3$ and the $\nu_1\nu_3$ PO $_4$ spectral domains. This obtained carbonate contents of 2.1, 4.0, and 5.4 wt% CO $_3^2$ in the Na-apatites, while the K-apatites exhibited rather close values of 2.4, 4.3, and 5.8 wt% CO $_3^2$, allowing for reasonable comparisons between the Na- and K-series.

For the Na-apatites in the ν_2 CO $_3$ region, the maximum peak position of A-type CO $_3^{2-}$ tended to slightly increase (blue-shift) from 878 to 879 cm $^{-1}$ as the total carbonate content increased (Fig. 4a). In contrast, there was a red-shift from 873.3 down to 871.9 cm $^{-1}$ for the B-type CO $_3^{2-}$ peak contribution upon increasing CO $_3^{2-}$ concentration. Finally, the band associated with the labile CO $_3^{2-}$ species in the 2 wt% CO $_3^{2-}$ apatite sample was positioned at 866 cm $^{-1}$, which upshifted to 867 cm $^{-1}$ for the 4% and 5.4% CO $_3^{2-}$ apatites. There was no measurable trend in the position of the HPO $_4^{2-}$ associated peak with increasing total CO $_3^{2-}$ content.



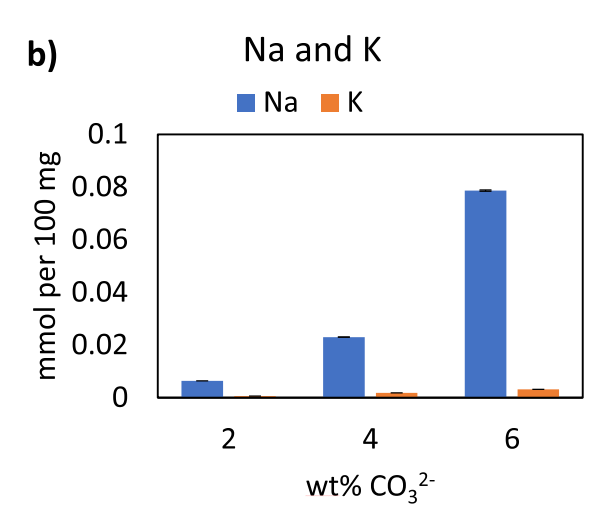


Fig. 3. Na⁺ and K⁺ substituted into biomimetic apatites. (a) Calcium, (b) sodium, and potassium content increased as increasing total wt% carbonate increased for Na- and K-apatites. Error bars represent instrumental errors.

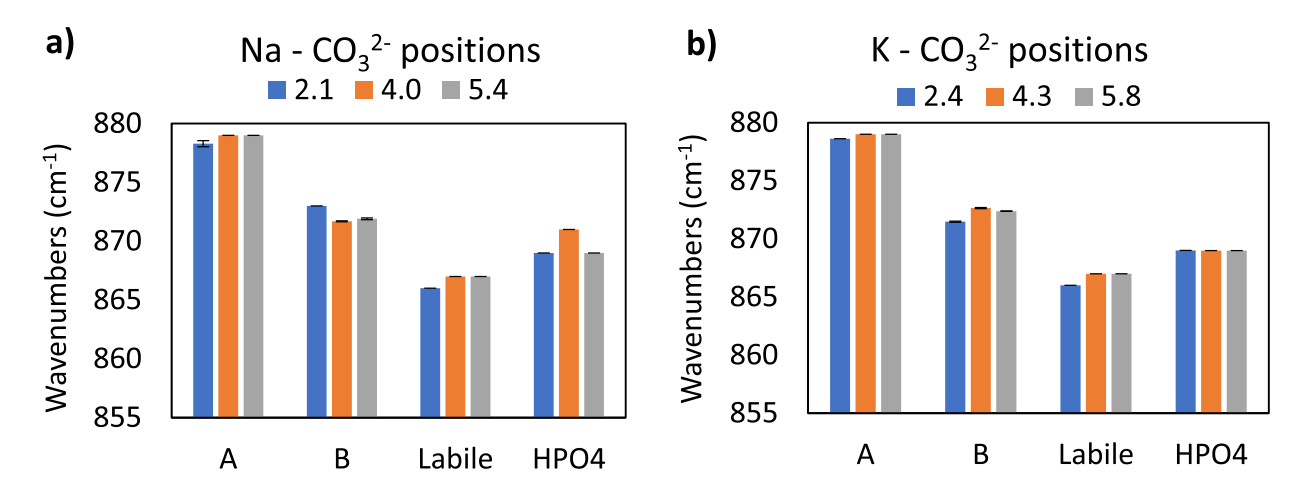


Fig. 4. Peak positions in the ν_2 CO $_3$ domain. Wavenumbers of the peak center for each carbonate type (A-type, B-type, labile) and total HPO $_4^{2-}$ in the (a) Na-apatites and (b) K-apatites.

For K-apatites, the A-type positions (879.6, 879, 879 cm $^{-1}$) remained essentially unchanged as the total CO_3^2 increased. For B-type CO_3^2 , there was a slight blue-shift trend (871.5, 872.7, 872.4 cm $^{-1}$) as the total CO_3^2 concentration increased (Fig. 4b). For labile CO_3^2 , the peak positions also slightly increased (866, 867, 867 cm $^{-1}$) while the HPO $_2^2$ -associated peak positions stayed the same (869 cm $^{-1}$) with increasing total CO_3^2 .

The deconvoluted peak areas for each type of CO_3^{2-} were used to determine the relative quantities of each. For all apatites, there was a

general increase of A-type CO_3^2 as the total wt% CO_3^2 increased. The percentage of A-type CO_3^2 in the Na-apatites was 0.48–0.94% while the range for K-apatites was 0.38–1.52 wt% (Fig. 5a). Although the amount of A-type CO_3^2 — was not significant between the Na- and K-apatites in 2 wt% CO_3^2 —, K-apatites had considerably more A-type CO_3^2 — at 4.3 and 5.8 wt% total CO_3^2 — than Na-apatites.

The B-type CO_3^{2-} spectral contribution also increased for all apatites with increasing total CO_3^{2-} . K-apatite had higher wt% of B-type CO_3^{2-} (1.34 wt%) than Na-apatite (0.99 wt%) at 2% total CO_3^{2-} values (Fig. 5b).

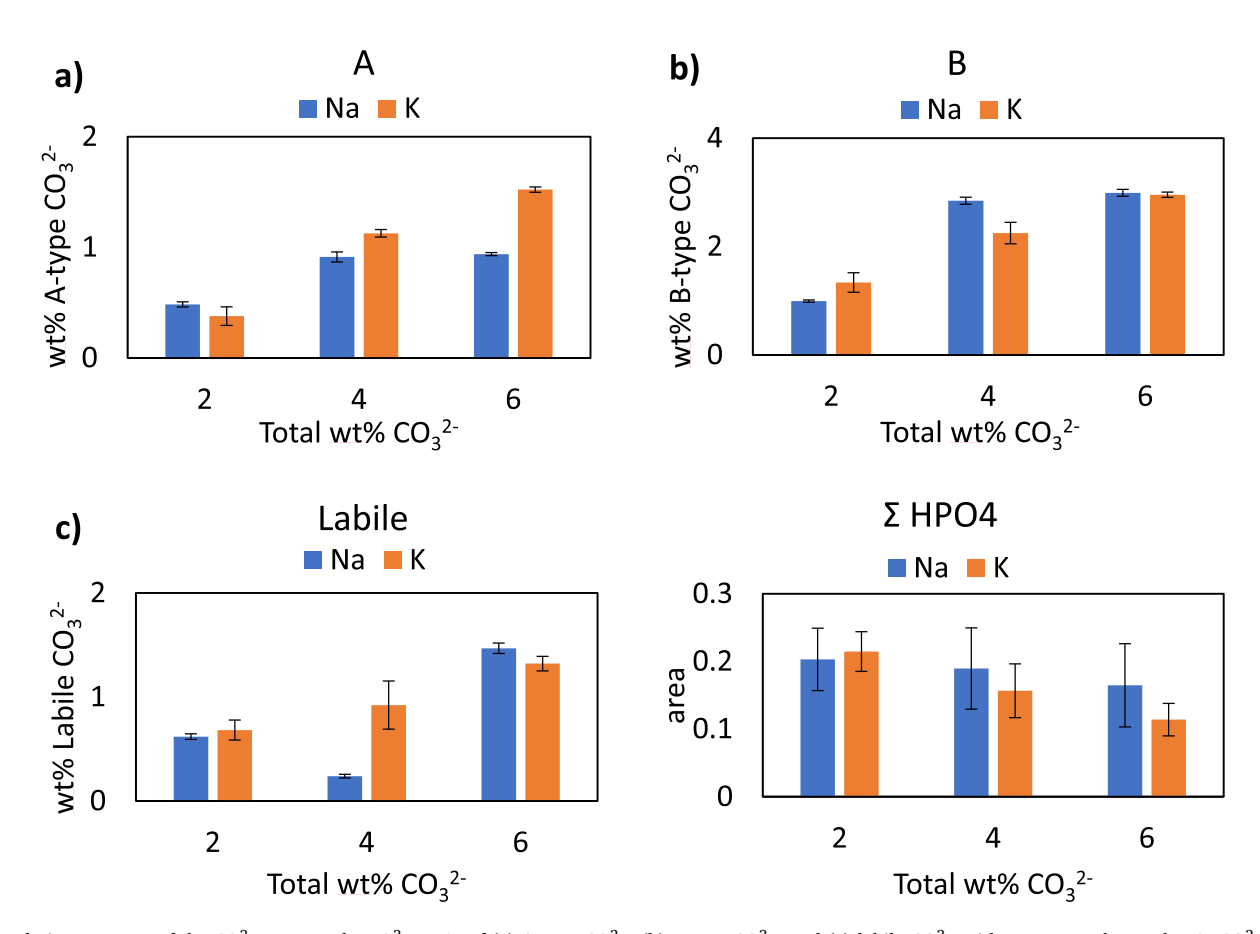


Fig. 5. Relative amounts of the CO_3^{2-} types and HPO_4^{2-} . wt% of (a) A-type CO_3^{2-} , (b) B-type CO_3^{2-} , and (c) labile CO_3^{2-} with respect to the total wt% CO_3^{2-} in Napatites and K-apatites. (d) The normalized area of the total HPO_4^{2-} content includes the non-apatitic and apatitic HPO_4^{2-} .

However, Na-apatites had slightly higher wt% of B-type CO_3^2 - (2.85% for Na-apatites) compared to the K-apatites (2.99%) at 4 wt% total CO_3^2 -. For 6 wt% CO_3^2 -, both Na- and K-apatites had similar B-type content (2.99% for Na-apatites vs 2.96% for K-apatites).

Concerning surface (labile) CO_3^2 , K-apatites had increasing labile CO_3^2 as the total wt% CO_3^2 increased. Na-apatites overall had an increasing trend, however, 4 wt% total CO_3^2 had less labile CO_3^2 (0.24%) than 2 wt% CO_3^2 (0.62%) (Fig. 5c). Comparing the Na- and K-series of samples, K-apatites exhibited higher amounts of labile CO_3^2 than Na-apatites at 4 wt% total CO_3^2 (0.92% vs 0.24%), while both Na- and K-apatites had similar values of labile CO_3^2 at 2 wt% (0.62 and 0.68, respectively) and 6 wt% CO_3^2 (1.47 and 1.32, respectively).

Upon increasing the total CO_3^{2-} content of the samples, all apatites experienced a general decrease in total HPO_4^{2-} , which includes the nonapatitic HPO_4^{2-} ions in the hydrated surface layer as well as the HPO_4^{2-} ions in the apatitic crystalline core of the nanocrystals (Fig. 1). While there was no obvious trend between Na- and K-apatites, the change in HPO_4^{2-} (ΔHPO_4) as CO_3^{2-} increased was more substantial in K-apatites ($\Delta = 0.058$ and 0.043) than Na-apatites (0.014 and 0.025) regarding the differences between 2%/4% and 4%/6%, respectively (Fig. 5d).

3.4. XRD

XRD analyses confirmed that all precipitated powders exhibited the characteristic apatite and bone-like pattern (Sup. Fig. 2a–c). For all apatites, the p-spacing of the (002) planes increased as CO_3^2 content increased in which Na- and K-apatites showed similar p-spacings (Fig. 6a). The (310) peak p-spacing generally decreased for the Na-apatites while the p-spacing increased for K-apatites as wt% CO_3^2 increased (Fig. 6b). Comparing Na- and K-apatites, the (310) p-spacing

was only slightly smaller for K-apatite at 2 wt% total CO_3^2 than Na-apatite (difference of 0.0026 Å); however, the p-spacing was higher for K-apatites than Na-apatites by 0.0068 and 0.0045 Å at 4% and 6% CO_3^{2-} , respectively.

The Na-apatites generally exhibited increased crystallite length and width along the (002) and (310) planes, respectively (Fig. 6c-d). There was no apparent trend with the crystallite size for the K-apatite series (Fig. 6c-d). Na- and K-apatites had similar crystallite lengths (10.10 vs 11.37 nm, respectively) and widths (3.44 vs 3.73 nm, respectively) at 2 wt% total CO_3^2 . At 4% total CO_3^2 , the K-apatite crystallite length and width was 4.68 and 1.69 nm larger than Na-apatite at the same wt% CO_3^2 . However, the opposite trend occurred for 6 wt% CO_3^2 where the Na-apatite crystallite length was 4.80 nm larger than that of the 6 wt% total CO_3^2 K-apatite.

4. Discussion

Bone and dentin apatites as well as their biomimetic synthetic analogs share several key features such as nonstoichiometry, nanosized crystal dimensions, and the presence of an ionic hydrated layer (amorphous and non-apatitic) covering the apatite nanocrystals. These compounds are significantly different in structure from regular, well-crystallized stoichiometric hydroxyapatite (HA) as for synthetic samples prepared at high temperature/pressure or in mature tooth enamel. Besides structural distinctions, compositional modifications are also involved, as biological apatite is formed and constantly submerged in body fluids rich in a large variety of inorganic ions – including those resulting from alimentation – leading to different degrees of ionic substitutions either in the apatitic core or within the amorphous surface layer on the nanocrystals. The ions present in this non-apatitic surface

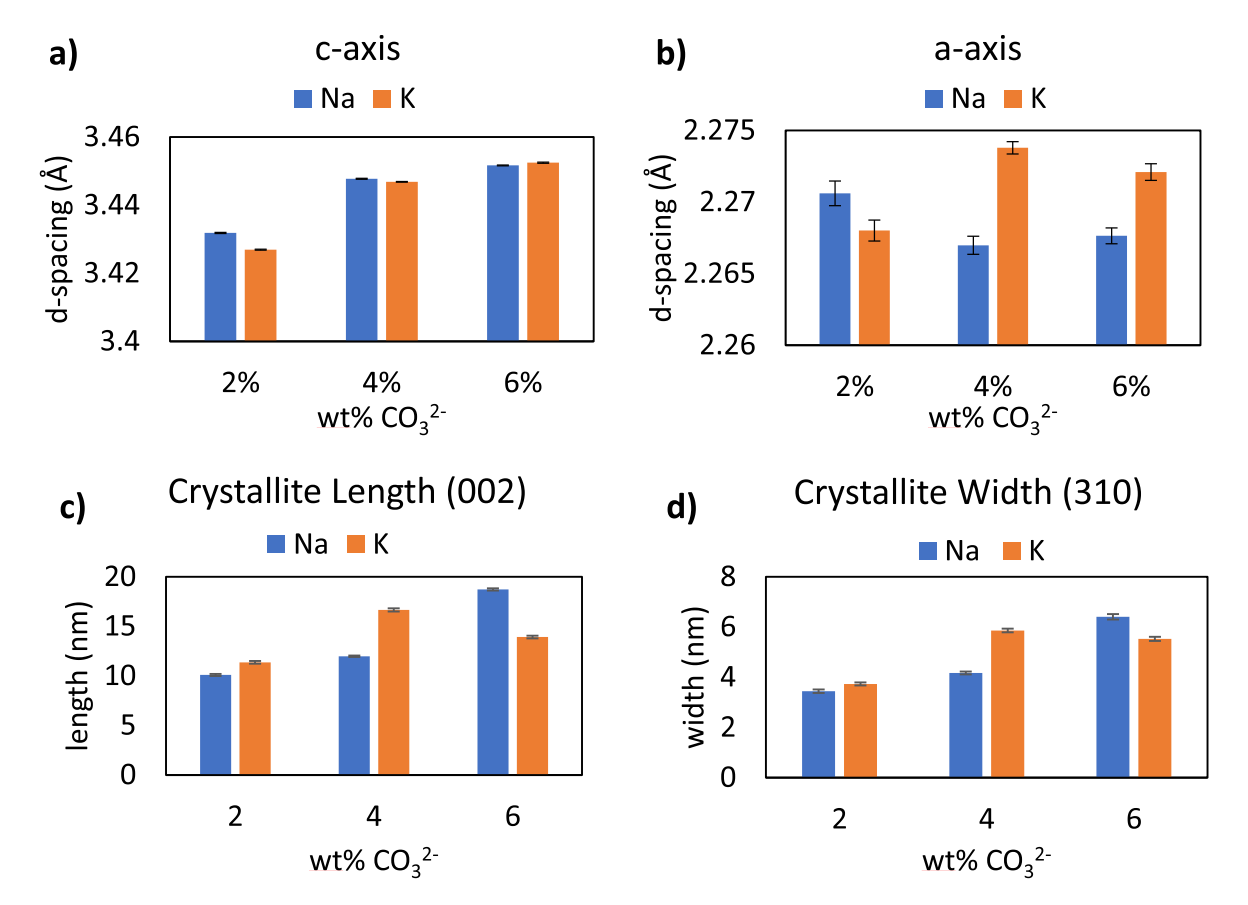


Fig. 6. Structural properties of the Na- and K-apatites. Values of p-spacings for the (a) (002) and (b) (310) diffraction lines for Na- and K-apatites with increasing wt $\% \text{ CO}_3^{2-}$. (c, d) The crystallite length and width were determined from the (002) and (310) through Scherrer's equation. Error bars for the c- and a-axis represent the standard error of the fitting parameters from Diffrac.eva. The error bars for crystallite length and width were calculated through propagation of error.

layer were shown previously to be highly labile and can be exchanged with ions contained in the surrounding fluids [22,49], depending on the nature of ion [18]. This mechanism is biologically relevant for maintaining adequate ionic concentrations in body fluids for homeostatic processes [50]. Thus, biological minerals may be considered as dynamic inorganic materials – far from the idea of an inert piece of stone.

This dynamic character depends on the overall thermodynamic stability of the bioapatite compound. The thermodynamic stability of nanocrystalline apatites has been quantitatively demonstrated to depend on its degree of nonstoichiometry [17]. This may be explained by the lower 3D cohesion of an apatitic lattice containing more ionic vacancies. In vivo as well as in biomimetic analogs, nanocrystalline apatites progressively undergo a maturation process with time spent in wet conditions [51,52]. A mechanistic scheme has been proposed for this maturation process for non-carbonated compounds, suggesting the progressive release of phosphate ions through the deprotonation of HPO_4^{2-} ions upon apatite aging in solution [22]. However, research is still in progress for carbonated compounds in terms of thermodynamic status and evolution through maturation. The ionic hydrated layer present on the nanocrystals - which is rich in calcium, water, and divalent anionic species such as HPO_4^{2-} ions or CO_3^{2-} – could be seen as an out-of-equilibrium interphase between the crystal surface and the surrounding liquid medium. The exact role of carbonation throughout the maturation process as well as the hydrated layer is still rather unknown, and this is further complicated by the co-presence of other ions, such as Na⁺ or K⁺.

For non-stoichiometric apatites, it is often considered as a first approximation that each Ca²⁺ vacancy in the lattice may be compensated by a concurrent vacancy in the OH⁻ site and the simultaneous protonation of a PO_4^{3-} ion into HPO_4^{2-} for charge balance [53,54]. Although a deeper examination of the charge compensation mechanism in highly immature apatites still needs to be evaluated - especially to account for the Ca and (H)PO₄ ions involved in the hydrated layer – this mechanistic scheme agrees with the main alterations of bioapatite or their synthetic biomimetic analogs, namely the significantly lower hydroxylation level as well as the large presence of HPO₄²⁻ ions [55]. In carbonated systems, it is then suggested that these divalent HPO₄²⁻ ions can be partly substituted by CO_3^{2-} in a similar mechanism [53]. Although this process is being further validated, especially for highly immature apatites, this provides a valuable first approximation of the observed compositional trends in bone-like apatites. However, additional charge balancing mechanisms may also come into play when monovalent cations, such as Na⁺ or K⁺, are also present in the medium, in which Na⁺/K⁺ could substitute for Ca²⁺ to account for some of the CO_3^{2-} -for- PO_4^{3-} substitution (B-type) [12,34,35].

In terms of relative amounts, it has been well established that CO_3^{2-} substitution is one of the primary physiological ionic substitutions in biological apatites and can have significant effects on their properties, such as increased solubility and resorption rates in biological conditions with increasing wt% CO_3^{2-} [13,24,25,56]. B-type CO_3^{2-} is generally considered to be the primary substitution in biological mineral, however, other types of CO_3^{2-} species are also involved in biological apatite and its synthetic analogs, such as A-type or labile surface CO_3^{2-} [21,23]. Na⁺ substitution is likely due to its prevalence in body fluids as well as some synthetic precipitating solutions. It may be noted that Na⁺ exhibits a somewhat larger ionic size than Ca^{2+} (Table 1) but still closer than other cations, such as K^+ , which are significantly more voluminous [35]. In the present study, we sought to elucidate the structural and chemical effects of monovalent substitutions by Na⁺ and K^+ in biomimetic carbonated apatites.

As evidenced by XRD and FTIR analyses (Sup. Fig. 1a-b, Sup. Fig. 2a-b), carbonated apatites with targeted levels of 2, 4, and 6 wt% $CO_3^{2^-}$ were successfully prepared by aqueous precipitation, in the presence of either K^+ or Na^+ used as counterions of precursor salts. This increase in $CO_3^{2^-}$ from 2 to 6 wt% suggests that the resorption rate *in vivo* may be increased irrespective of Na^+ and K^+ substitutions [56]. As total $CO_3^{2^-}$

levels increased for the Na- and K-apatites, the monovalent cationic content concurrently increased. This supports the idea that monovalent cations co-substitute with CO_3^{2-} to maintain charge balance [12,27]. However, the Na-apatites exhibited $10 \times, 12.3 \times, \text{ and } 24.8 \times \text{more Na}^+$ than K⁺ in the K-apatites for 2, 4, and 6 wt% total CO₃² (Fig. 3b). This confirmed that Na⁺ integrated into the apatite structure much more effectively than K⁺. These findings are in agreement with previous observations [21,44]. This is likely due to a greater mismatch of ionic sizes between K⁺ and Ca²⁺ compared to Na⁺/Ca²⁺ [32,33]. However, there is evidence that a lower Gibbs free binding energy for K⁺ would make K⁺ more thermodynamically favorable for substitution compared to Na⁺ due to its reduced electronegativity (0.82 vs 0.93) and higher Metal-Oxygen (M-O) bond character (1.445 vs 1.375) [18]. This suggests that cationic size and even electronegativity may not be the sole factors that allow metal ions to substitute into biomimetic apatites, and local constraints as well as symmetry may also come into play [14,46]. Thus, despite the seemingly favorable thermodynamic drive for K⁺ substitution, the mechanical constraints imposed on the lattice during the substitution likely serve to regulate cationic inclusion. As cationic and anionic substitutions increased, both the Na- and K-apatite unit cells experienced an increased c-axis parameter as seen by the increased (002) p-spacing. This suggests that these substitutions caused an expansion of the lattice along the c-axis. In the Na-apatites, the perpendicular a-axis parameter related to the (310) plane decreased with increasing substitution (Fig. 6b). This has been commonly seen in B-type CO_3^2 substitution, where CO_3^2 exchanges for PO_4^{3-} , causing c-axis expansion and a-axis contraction [13,24]. Our FTIR data further confirmed that the Na-apatites were primarily B-type apatites with lower levels of A-type CO_3^{2-} (Fig. 5b). On the other hand, K^+ increased the a-axis D-spacing for the same total CO_3^{2-} substitution. This suggests that K⁺ substitution significantly expanded the lattice along all axes of the unit cell despite the low amount of K⁺ incorporation (Fig. 7b). Accounting for both axes, the presence of K+ led to a 0.6% greater expansion in the unit cell total volume at 4 wt% CO₃²-than Na⁺ (46.30 nm³ vs. 46.03 nm³). This may be partly caused by the significantly larger cationic radius of K⁺; however, an increased a-axis in apatite may also be associated with A-type CO_3^{2-} substitutions. Examination of the FTIR data supports both theories, as the K-apatites were primarily B-type CO_3^2 substituted but they also contained significantly higher amounts of A-type CO_3^{2-} than the Na-apatites. Together, these results indicate that cationic substitutions affect the unit cell structure not alone, but in conjunction with their effects on CO_3^2 -substitutions.

To further explore how K^+ and Na^+ substitutions affected CO_3^{2-} in the apatite, the FTIR data corresponding to the out-of-plane v2 CO3 deformation mode were analyzed (Fig. 2b). Na-apatites showed a red-shift in bond energy for the main carbonate type, B-type CO_3^{2-} , with increasing substitutions. To the best of our knowledge, such a shift has not yet been reported in bone-like apatites, but a comparative analysis of several carbonated salts in the literature showed a downshift of ν_2 CO₃ for carbonates located in disorganized structures (e.g. for amorphous/ vitrous states) [27]. This was correlated to weaker binding due to a "disruption of the local intermediate-scale structure" [27]. This may be linked to local constraints within the unit cell, and our XRD findings of the changes in unit cell parameters for the partial Na-for-Ca substitution indeed suggest the existence of locally distorted crystalline sites. To shed more light on the local CO₃² modifications in bone-like Na-bearing apatite compounds, analysis of the asymmetric stretching v_3 CO₃ mode was also evaluated by FTIR (Sup. Fig. 1a-b). In this spectral domain, each CO₃² type leads to a doublet signal that ultimately generates a very complex multicomponent band as previously stated in Section 2.3. This complexity is further enhanced by the fact that these apatites have a combination of A- and B-type CO_3^{2-} substitutions, and the different CO_3^{2-} types may "sense" each other, especially with increasing total CO_3^{2-} levels, which may lead to additional lattice bands and band assignment ambiguity [27]. However, it is fortunate that the most intense low-frequency limb of the ν_3 CO₃ domain (around 1415–1420 cm⁻¹) is

(Hydroxy)apatite unit cell / CO₃ increased incorporation

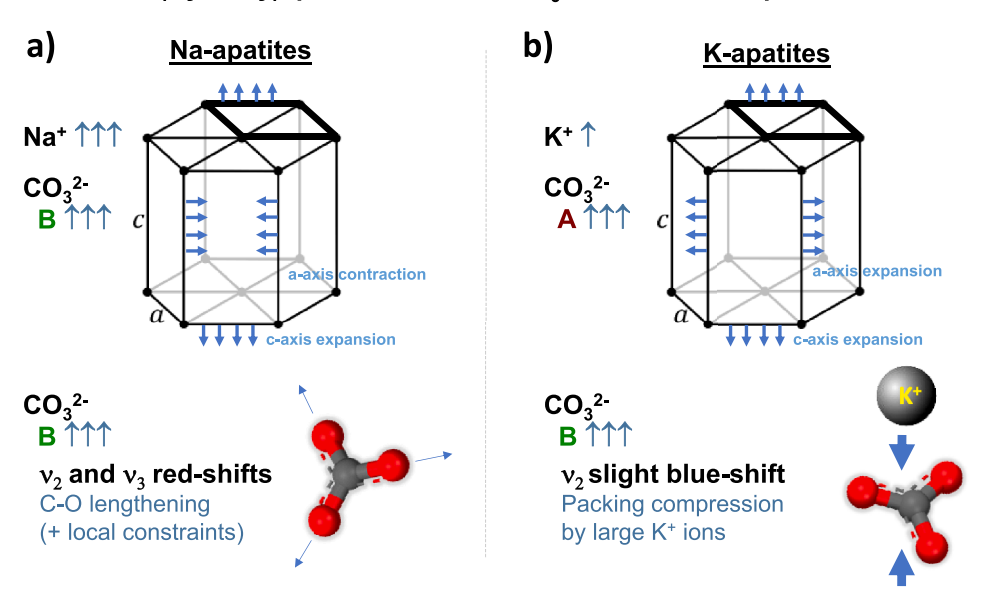


Fig. 7. Schematic of the unit cell when Na $^+$ or K $^+$ is co-substituted with CO_3^{2-} . (a) Na-apatites increased in Na $^+$ and B-type CO_3^{2-} , causing the c-axis to expand and a-axis to contract. The FTIR wavenumbers for B-type CO_3^{2-} red-shifted in both ν_2 CO $_3$ and ν_3 CO $_3$ domains, suggesting modified local constraints and lengthened C—O bond for Na/CO $_3$ -apatites. (b) K-apatites contained K $^+$ and more A-type CO_3^{2-} than Na-apatites, leading to an expansion of both a-and c-axes. The wavenumber for B-type CO_3^{2-} in the ν_2 CO $_3$ mode exhibited a slight blue-shift, suggesting a size effect operated by the large K $^+$ ion (packing compression of carbonates) in K/CO $_3$ -apatites.

assigned to the B-type CO_3^{2-} contribution of interest here [27]. Interestingly, as for the ν_2 CO₃ deformation mode, a red-shift of the B-type CO_3^{2-} position could also be evidenced, typically from ca. 1419.4 cm⁻¹ down to ca. 1416.4 cm $^{-1}$, as total CO $_3^{2-}$ increased from 2 to 6 wt%. For a more accurate assessment, Fourier self-deconvolution processing (apodization) was applied to the whole ν_3 CO₃ domain to better resolve the contributions (Sup. Fig. 4a-f). The B-type CO_3^{2-} signal again confirmed the previous conclusions, pointing to a red-shift as CO_3^{2-} increased for the Na-series (Sup. Fig. 3a). The stretching nature of the ν_3 CO₃ vibration mode suggests a lengthening of the B-type C—O bond for our Na-bearing samples as the total CO_3^{2-} increased. The longer bond length may be due to the extra space provided within the lattice from the smaller CO_3^{2-} ion substituting into a bulky PO_4^{3-} space [57]. Regarding Na⁺, it is plausible that the Na⁺ ions may migrate to the vacant oxygen site of the phosphate that is closest to the OH channel to maintain optimal charge balance [57].

The same ν_2 CO₃ and ν_3 CO₃ domains analyses were evaluated for the K-apatite series. For v_2 CO₃, contrarily to the Na-samples, a slight blueshift was shown for B-type CO_3^2 (Fig. 4b). However, no clear trend was seen in the B-type CO_3^{2-} signature in the ν_3 CO_3 domain (Sup. Fig 3b). This may be due to either the low overall amount of K⁺ (thus, many Ca²⁺ neighboring cations remain present in this K-apatite samples) and/or no noticeable change occurred in the C-O bond length. The slight blueshift detected in the out-of-plane ν_2 CO₃ deformation domain is difficult to explain with certainty at this point. Other large cations, such as Sr²⁺, have been shown to potentially occupy both the Ca(I) and Ca(II) sites. However, Sr²⁺ may preferentially substitute for Ca²⁺ in the Ca(II) sites at high Sr²⁺ contents as these sites provide the largest volume for the large ion as opposed to the Ca(I) sites [58]. Yet, at low Sr content, a slight preference for Ca(I) seems to be observed [58]. A similar scenario may occur here, in which K⁺ may substitute for the Ca(I) site at our low doping rates. This would mostly affect the neighboring phosphate sites, or B-type CO_3^{2-} , leading to altered constraints for the CO_3^{2-} ions as opposed to Na-apatites. In addition, the wavenumber increases in a crystalline environment compared to the free CO₃²⁻ ion, which may arise from the effect of a packing compression among the neighboring cations [48]. A similar phenomenon could be involved in this study with substituting K⁺ ions playing a packing-enhancement role. In any case, our XRD data demonstrated different structural changes in the unit cell geometry between Na⁺ and K⁺, and the larger amount of Ca²⁺ neighbors near CO_3^{2-} ions for the K-apatites compared to Na^+ may also contribute to different unit cell distortion mechanisms.

As mentioned previously, biological apatite and biomimetic analogs also have a hydrated surface layer on the nanocrystals that possesses variations in cationic and anionic concentrations with chemical and structural differences [55,59,60]. For K-apatites and Na-apatites, labile $\mathrm{CO}_3^{2^-}$ generally increased and the overall amount of $\mathrm{HPO}_4^{2^-}$ (apatitic and non-apatitic) decreased as the total $\mathrm{CO}_3^{2^+}$ content increased. These opposite trends are associated with maturation of biological carbonated apatites, where increased aging in bone apatite causes more labile carbonate while simultaneously decreasing $\mathrm{HPO}_4^{2^-}$ contents [1,49,61]. These results agree with the maturation times shown in Table 2. Note that the band around 866 cm⁻¹ assigned to the labile surface $\mathrm{CO}_3^{2^-}$ should not be confounded for the specific band observed in the same region by Fleet [27] on apatites obtained by high temperature and pressure, as these are assigned to a particular local organization denoted as "A2" of A-type carbonates.

This evolution of the relative labile CO_3^{2-} amounts was accompanied by a slight blue-shift of their ν_2 CO₃ mode as total CO₃²-substitutions increased for both Na- and K-apatites. If we make a parallel with the comparative literature study of carbonate salts cited above [27], this slight blue-shift may be tentatively associated with an even lower degree of ionic organization within the hydrated layer as CO_3^{2-} levels increased. This may be linked to the "missing" oxygen in the CO_3^{2-} ion compared to the tetrahedral HPO₄²⁻ ion that is replaced within the surface layer (further disorganizing the hydrogen bonding network of the H₂O molecules present in the layer). The K-apatites showed stronger effects in all these parameters than the Na-apatites, which may be due to the longer and higher maturation times and temperatures needed to prepare the K-apatites. The higher retention of HPO₄²⁻ with Na⁺ may result from two reasons: (1) the charge balancing mechanism for B-type CO_3^{2-} may be occurring [62,63] and/or (2) Na+ may help maintain well-developed HPO_4^{2-} layers in apatite as seen in octacalcium phosphate [64,65]. To our knowledge, this is the first study to probe the function of Na⁺ and K⁺ on the hydrated layer in biomimetic apatites.

4.1. Limitations

The interplay between maturation, temperature, and the initial CO_3^{2-}/PO_3^{4-} molar ratio in the starting reagents used in the synthesis

methods may have affected the structural properties, such as crystallite size [45]. The maturation process allows for increased crystallite size as well as progressive CO_3^{2-} incorporation [66] as seen in the Na-apatites [39]. Increased temperatures typically accelerate the maturation process crystallite size as well, as shown in the $2-6\% \text{ CO}_3^{2-}$ (Fig. 6c-d) [45]. However, the crystallite size did not increase with increasing CO_3^{2-} for the K-apatites, despite the higher temperature and longer maturation times used for this series (Table 2). This suggests that CO_3^{2-} in conjunction with K⁺ may have affected crystal growth formation. CO₃²⁻ is a known crystal growth inhibitor [67,68] and K⁺ has been reported to inhibit nucleation and crystal growth as well [69,70]. This inhibition was revealed in the 6 wt% CO_3^{2-} K-apatite due to the higher CO_3^{2-}/PO_4^{3-} molar ratio compared to the lower wt% CO_3^{2-} apatites (2:1 for 6% vs 1:1 for 2/4%) (Table 2). In addition, identical synthesis parameters were used for 4% CO_3^{2-} Na-apatite and 2% CO_3^{2-} K-apatite as well as 6% CO_3^{2-} Na-apatite and 4% CO_3^{2-} K-apatite. When purely comparing Na- and K-apatites based on the synthesis conditions, K-apatites have less CO_3^{2-} and generally smaller crystallite length and width (Fig. 6c-d). This suggests that K⁺ may influence the structural properties of apatites in addition to CO_3^{2-} . Future studies parsing out the individual effects of maturation, temperature, and CO_3^{2-}/K^+ inhibition will be important to further identify their precise contributions on K-containing carbonated apatites.

5. Conclusions

In this study, we prepared biomimetic carbonated apatites in Na- or K-rich solutions, with three CO₃²⁻ levels relevant to bone. While Na⁺ more readily substituted for Ca²⁺ in our close-to-physiological precipitation conditions, K⁺ scarcely incorporated into the structure. Yet, both Na^+ and K^+ co-substitutions with CO_3^{2-} were shown to modify the physicochemical features of the precipitated apatites. To date, potassium's function had been overlooked in the literature; however, we reveal that K⁺ co-substitution, even in limited quantity, affects the unit cell parameters and the local ionic environments. This could impact the regulation of water absorption, CO_3^{2-} reactivity, and CO_3^{2-} mobility in apatites [25,71]. Overall, the data shown here indicate that Na⁺ and K⁺ have distinct mechanisms for CO₃²-incorporation during apatite crystallization and ionic exchange in Na⁺ and K⁺-rich solutions. The relative amounts of A-, B- and labile-type CO_3^{2-} were assessed by deconvolution of the IR-active v_2 CO₃ domain while taking into account – as is rarely done – the presence of the underlying HPO₄²⁻ spectral contribution. These relative amounts were found to vary depending on the nature of the substituting monovalent cation and overall CO_3^{2-} level. Understanding the effect of monovalent cations on the amount of A-, B-, or labile CO_3^{2-} could help elucidate how the seemingly unfavorable A-type CO₃²⁻ incorporation into apatite occurs biologically at atmospheric pressure. Also, we show that the CO₃-for-(H)PO₄ substitution pathway (B-type CO_3^{2-}) in the co-presence of Na⁺ led to a lengthening (weakening) of the C—O bond, as shown by analysis of the ν_3 CO₃ vibrational domain. Furthermore, the role of the local structural constraints was demonstrated and differentiated between the Na/CO₃²⁻ and K/CO₃²⁻ substitution mechanisms based on FTIR and XRD data.

From a more fundamental viewpoint, we report new data using bone-like nanocrystalline apatites synthesized in close-to-physiological temperatures. The FTIR analyses shown here, especially for Na/CO $_3^{2-}$ co-substituted apatites, are distinct from previous studies utilizing apatites prepared at high temperature and/or pressure that may have other types of structural changes than those expected *in vivo*. From a biomedical engineering perspective, by taking advantage of carbonate's ability to inhibit apatite crystal growth, using these ions may help further tune the hydrated layer's reactivity/stability. In addition, the presence of K⁺ or Na⁺ may help modulate the resorption rate of carbonate apatite-based bone substitutes after implantation, allowing for different behaviors *in vivo*. This work will also add to the existing repertoire on controlling CO_3^{2-} incorporations for clinical treatment and

biomedical applications. Overall, our findings suggest that biological apatite in the body can change/adapt its material properties during high influxes of Na⁺ or K⁺ in body fluids. This may resonate in the field of biomineralization research to help understand normal and/or pathological calcification behaviors *in vivo*.

Declaration of Competing Interest

The authors declare that they have no known competing financial interests or personal relationships that could have appeared to influence the work reported in this paper.

Acknowledgments

Funding was provided by the Chateaubriand Fellowship for Stephanie Wong; the NSF CAREER [grant number 2044870] for Alix Deymier; and CIRIMAT's internal financial resources for Chris Drouet. We would like to thank Edoardo Cianflone and David Bertrand, both from CIRIMAT France, for their assistance in the atomic absorption work.

Supplementary materials

Supplementary material associated with this article can be found, in the online version, at doi:10.1016/j.mtla.2023.101795.

References

- C. Rey, C. Combes, C. Drouet, H. Sfihi, A. Barroug, Physico-chemical properties of nanocrystalline apatites: implications for biominerals and biomaterials, Mater. Sci. Eng. C 27 (2007) 198–205, https://doi.org/10.1016/j.msec.2006.05.015.
- [2] F. Bertolotti, F.J. Carmona, G. Dal Sasso, G.B. Ramírez-Rodríguez, J.M. Delgado-López, J.S. Pedersen, F. Ferri, N. Masciocchi, A. Guagliardi, On the amorphous layer in bone mineral and biomimetic apatite: a combined small- and wide-angle Xray scattering analysis, Acta Biomater. (2020), https://doi.org/10.1016/j. actbio.2020.04.026
- [3] S. Von Euw, T.H.C. Chan-Chang, C. Paquis, B. Haye, G. Pehau-Arnaudet, F. Babonneau, T. Azaïs, N. Nassif, Organization of bone mineral: the role of mineral-water interactions, Geosciences 8 (2018) 1–18, https://doi.org/10.3390/ geosciences8120466 (Basel) (Switzerland.
- [4] D. Eichert, C. Combes, C. Drouet, C. Rey, Formation and evolution of hydrated surface layers of apatites, Key Eng. Mater. 284–286 (2005) 3–6, https://doi.org/ 10.4028/www.scientific.net/kem.284-286.3.
- [5] N. Tokonami, D. Mordasini, S. Pradervand, G. Centeno, C. Jouffe, M. Maillard, O. Bonny, F. Gachon, R.A. Gomez, M.L.S. Sequeira-Lopez, D. Firsov, Local renal circadian clocks control fluid–electrolyte homeostasis and BP, JASN 25 (2014) 1430–1439, https://doi.org/10.1681/ASN.2013060641.
- [6] M.J. Hannon, J.G. Verbalis, Sodium homeostasis and bone, Curr. Opin. Nephrol. Hypertens. 23 (2014) 370–376, https://doi.org/10.1097/01. mph 0000447022 51722 fd
- [7] L.A. Frassetto, R.C. Morris, D.E. Sellmeyer, A. Sebastian, Adverse effects of sodium chloride on bone in the aging human population resulting from habitual consumption of typical American diets, J. Nutr. (2008) 419–422, https://doi.org/ 10.1093/in/138.2.419.
- [8] V.K. Bansal, Serum Inorganic Phosphorus, Clinical Methods: The History, Physical, and Laboratory Examinations. (1990). https://www.ncbi.nlm.nih.gov/books/NBK310/ (accessed May 30, 2022).
- [9] T. Aoba, The effect of fluoride on apatite structure and growth, Crit. Rev. Oral Biol. Med. 8 (1997) 136–153, https://doi.org/10.1177/10454411970080020301.
- [10] C. Robinson, R.C. Shore, S.J. Brookes, S. Strafford, S.R. Wood, J. Kirkham, The chemistry of enamel caries, Crit. Rev. Oral Biol. Med. 11 (2000) 481–495, https:// doi.org/10.1177/10454411000110040601.
- [11] D.G.A. Nelson, J.D.B. Featherstone, J.F. Duncan, T.W. Cutress, Effect of carbonate and fluoride on the dissolution behaviour of synthetic apatites, Caries Res. 17 (1983) 200–211, https://doi.org/10.1159/000260668.
- [12] A. Bigi, E. Boanini, M. Gazzano, Ion substitution in biological and synthetic apatites. Biomineralization and Biomaterials, Elsevier, 2016, pp. 235–266, https://doi.org/10.1016/B978-1-78242-338-6.00008-9.
- [13] A.C. Deymier, A.K. Nair, B. Depalle, Z. Qin, K. Arcot, C. Drouet, C.H. Yoder, M. J. Buehler, S. Thomopoulos, G.M. Genin, J.D. Pasteris, Protein-free formation of bone-like apatite: new insights into the key role of carbonation, Biomaterials 127 (2017) 75–88. https://doi.org/10.1016/j.biomaterials.2017.02.029.
- [14] J.F. Cawthray, A.L. Creagh, C.A. Haynes, C. Orvig, Ion Exchange in Hydroxyapatite with Lanthanides, Inorg. Chem. 54 (2015) 1440–1445, https://doi.org/10.1021/ ic502425e.

- [15] E.A.P. De Maeyer, R.M.H. Verbeeck, I.Y. Pieters, Effect of K+ on the stoichiometry of carbonated hydroxyapatite obtained by the hydrolysis of monetite, Inorg. Chem. 35 (1996) 857–863, https://doi.org/10.1021/ic950916k.
- [16] S.M. Hosseini, C. Drouet, A. Al-Kattan, A. Navrotsky, Energetics of lanthanide-doped calcium phosphate apatite, Am. Mineralog. 99 (2014) 2320–2327, https://doi.org/10.2138/am-2014-4930.
- [17] S. Rollin-Martinet, A. Navrotsky, E. Champion, D. Grossin, C. Drouet, Thermodynamic basis for evolution of apatite in calcified tissues, Am. Mineralog. 98 (2013) 2037–2045, https://doi.org/10.2138/am.2013.4537.
- [18] C. Drouet, A comprehensive guide to experimental and predicted thermodynamic properties of phosphate apatite minerals in view of applicative purposes, J. Chem. Thermodyn. 81 (2015) 143–159, https://doi.org/10.1016/j.jct.2014.09.012.
- [19] M. Sydney-Zax, I. Mayer, D. Deutsch, Carbonate content in developing human and bovine enamel, J. Dent. Res. 70 (1991) 913–916, https://doi.org/10.1177/ 00220345910700051001.
- [20] S.V. Dorozhkin, M. Epple, Biological and medical significance of calcium phosphates, Angew. Chem. Int. Ed. 41 (2002) 3130–3146, https://doi.org/ 10.1002/1521-3773(20020902)41:17<3130::AID—ANIE3130>3.0.CO;2-1.
- [21] M.E. Fleet, X. Liu, Carbonate in synthetic and biological apatites, in: Proceedings of the 9th International Congress for Applied Mineralogy, 2008, pp. 303–311.
- [22] C. Drouet, M. Aufray, S. Rollin-Martinet, N. Vandecandelaère, D. Grossin, F. Rossignol, E. Champion, A. Navrotsky, C. Rey, Nanocrystalline apatites: the fundamental role of water, Am. Mineralog. 103 (2018) 550–564, https://doi.org/ 10.2138/am-2018-6415.
- [23] C. Rey, B. Collins, T. Goehl, I.R. Dickson, M.J. Glimcher, The carbonate environment in bone mineral: a resolution-enhanced Fourier transform infrared spectroscopy study, Calcif Tissue Int. 45 (1989) 157–164, https://doi.org/ 10.1007/BF02556059.
- [24] H. Madupalli, B. Pavan, M.M.J. Tecklenburg, Carbonate substitution in the mineral component of bone: discriminating the structural changes, simultaneously imposed by carbonate in A and B sites of apatite, J. Solid State Chem. 255 (2017) 27–35, https://doi.org/10.1016/j.jssc.2017.07.025.
- [25] F. Peccati, C. Bernocco, P. Ugliengo, M. Corno, Properties and reactivity toward water of a type carbonated apatite and hydroxyapatite surfaces, J. Phys. Chem. C 122 (2018) 3934–3944, https://doi.org/10.1021/acs.jpcc.7b12738.
- [26] T. Kubota, A. Nakamura, K. Toyoura, K. Matsunaga, The effect of chemical potential on the thermodynamic stability of carbonate ions in hydroxyapatite, Acta Biomater. 10 (2014) 3716–3722, https://doi.org/10.1016/j.actbio.2014.05.007.
- [27] M.E. Fleet, Carbonated Hydroxyapatite: Materials, Synthesis, and Applications, Jenny Stanford Publishing, 2014. https://books.google.com/books?id=RbD
- [28] H. Lodish, A. Berk, C. Kaiser, M. Krieger, A. Bretscher, H. Ploegh, K. Martin, M. Yaffe, A. Amon, Molecular Cell Biology, Macmillan Learning, 2021. https://books.google.com/books?id=adAIzgEACAAJ.
- [29] J.C. Elliott, Calcium phosphate biominerals, Rev. Mineral. Geochem. 48 (2002) 427–453, https://doi.org/10.2138/rmg.2002.48.11.
- [30] O.F. Yasar, W.C. Liao, R. Mathew, Y. Yu, B. Stevensson, Y. Liu, Z. Shen, M. Edén, The carbonate and sodium environments in precipitated and biomimetic calcium hydroxy-carbonate apatite contrasted with bone mineral: structural insights from solid-state NMR, J. Phys. Chem. C 125 (2021) 10572–10592, https://doi.org/ 10.1021/ACS.JPCC.0C11389.
- [31] T. Georges, Compréhension Des Premières étapes de Nucléation De L'apatite Biologique, Sorbonne Université, 2023.
- [32] H.E. Mason, A. Kozlowski, B.L. Phillips, Solid-state NMR study of the role of H and Na in AB-type carbonate hydroxylapatite, Chem. Mater. 20 (2008) 294–302, https://doi.org/10.1021/cm0716598.
- [33] M.E. Fleet, Infrared spectra of carbonate apatites: evidence for a connection between bone mineral and body fluids, Am. Mineralog. 102 (2017) 149–157, https://doi.org/10.2138/am-2017-5704.
- [34] C.H. Yoder, K.R. Stepien, T.M. Edner, A new model for the rationalization of the thermal behavior of carbonated apatites, J. Therm. Anal. Calorim. 140 (2020) 2179–2184, https://doi.org/10.1007/s10973-019-08946-7.
- [35] R.D. Shannon, Revised effective ionic radii and systematic studies of interatomic distances in halides and chalcogenides, Acta Cryst. A 32 (1976) 751–767, https://doi.org/10.1107/S0567739476001551.
- [36] J.G. Speight, Lange's Handbook of Chemistry, 16th ed., McGraw-Hill, Laramie, Wyoming, 2022.
- [37] T. Tite, A.C. Popa, L. Balescu, I. Bogdan, I. Pasuk, J. Ferreira, G. Stan, Cationic substitutions in hydroxyapatite: current status of the derived biofunctional effects and their in vitro interrogation methods, Materials 11 (2018) 2081, https://doi. org/10.3390/ma11112081 (Basel).
- [38] M.E. Fleet, X. Liu, Coupled substitution of type A and B carbonate in sodiumbearing apatite, Biomaterials 28 (2007) 916–926, https://doi.org/10.1016/j. biomaterials.2006.11.003.
- [39] C.H. Yoder, M.M. Bollmeyer, K.R. Stepien, R.N. Dudrick, The effect of incorporated carbonate and sodium on the IR spectra of A- and AB-type carbonated apatites, Am. Mineralog. 104 (2019) 869–877, https://doi.org/10.2138/am-2019-6800.
- [40] S. Peroos, Z. Du, N.H. De Leeuw, A computer modelling study of the uptake, structure and distribution of carbonate defects in hydroxy-apatite, Biomaterials 27 (2006) 2150–2161, https://doi.org/10.1016/j.biomaterials.2005.09.025.
- [41] E.A.P. De Maeyer, R.M.H. Verbeeck, Possible substitution mechanisms for sodium and carbonate in calciumhydroxyapatite, Bull. Des Soc. Chim. Belges 102 (1993) 601–609, https://doi.org/10.1002/bscb.19931020907.
- [42] F.C.M. Driessens, R.M.H. Verbeeck, H.J.M. Heijligers, Some physical properties of Na- and CO₃-containing apatites synthesized at high temperatures, Inorg. Chim. Acta 80 (1983) 19–23, https://doi.org/10.1016/S0020-1693(00)91256-8.

- [43] A.C. Tas, F. Aldinger, Formation of apatitic calcium phosphates in a Na-K-phosphate solution of pH 7.4, J. Mater. Sci. Mater. Med. 16 (2005) 167–174, https://doi.org/10.1007/s10856-005-5919-5.
- [44] R.M.H. Verbeeck, E.A.P. De Maeyer, F.C.M. Driessens, Stoichiometry of potassiumand carbonate-containing apatites synthesized by solid state reactions, Inorg. Chem. 34 (1995) 2084–2088, https://doi.org/10.1021/ic00112a021.
- [45] N. Vandecandelaere, C. Rey, C. Drouet, Biomimetic apatite-based biomaterials: on the critical impact of synthesis and post-synthesis parameters, J. Mater. Sci. Mater. Med. 23 (2012) 2593–2606, https://doi.org/10.1007/s10856-012-4719-y.
- [46] A. Grunenwald, C. Keyser, A.M. Sautereau, E. Crubézy, B. Ludes, C. Drouet, E. Crub Ezy C, B. Ludes, C. Drouet, Revisiting carbonate quantification in apatite (bio) minerals: a validated FTIR methodology, J. Archaeol. Sci. 49 (2014) 134–141, https://doi.org/10.1016/j.jas.2014.05.004.
- [47] C. Ortali, M. Vandenhende, C. Drouet, E. Champion, Consolidation of bone-like apatite bioceramics by spark plasma sintering of amorphous carbonated calcium phosphate at very low temperature, J. Eur. Ceram. Soc. 38 (2018) 2098–2109, https://doi.org/10.1016/j.jeurceramsoc.2017.11.051.
- [48] V.C. Farmer, The Infrared Spectra of Minerals, Mineralogical Society, 1974. https://books.google.com/books?id=IddPAQAAIAA.J.
- [49] C. Combes, S. Cazalbou, C. Rey, Apatite biominerals, Minerals 6 (2016) 34, https://doi.org/10.3390/min6020034.
- [50] D.A. Bushinsky, Acid-base imbalance and the skeleton, Eur. J. Nutr. 40 (2001) 238–244, https://doi.org/10.1007/s394-001-8351-5.
- [51] C. Rey, M. Shimizu, B. Collins, M.J. Glimcher, Resolution-enhanced Fourier transform infrared spectroscopy study of the environment of phosphate ions in the early deposits of a solid phase of calcium-phosphate in bone and enamel, and their evolution with age. I: investigations in the upsilon 4 PO4 domain, Calcif. Tissue Int. 46 (1990) 384–394. https://doi.org/10.1007/BF02554969.
- [52] C. Rey, M. Shimizu, B. Collins, M.J. Glimcher, Resolution-enhanced Fourier transform infrared spectroscopy study of the environment of phosphate ion in the early deposits of a solid phase of calcium phosphate in bone and enamel and their evolution with age: 2. Investigations in the nu3PO4 domain, Calcif. Tissue Int. 49 (1991) 383–388, https://doi.org/10.1007/BF02555847.
- [53] J.C. Elliot, Mineral, synthetic and biological carbonate apatites. Structure and Chemistry of the Apatites and Other Calcium Orthophosphates, 1st ed., 1994, pp. 191–304.
- [54] J.C. Elliot, Hydroxyapatite and nonstoichiometric apatites. Structure and Chemistry of the Apatites and Other Calcium Orthophosphates, 1st ed., 1994, pp. 111-189.
- [55] S. Von Euw, Y. Wang, G. Laurent, C. Drouet, F. Babonneau, N. Nassif, T. Azaïs, Bone mineral: new insights into its chemical composition, Sci. Rep. 9 (2019) 1–11, https://doi.org/10.1038/s41598-019-44620-6.
- [56] K. Deguchi, S. Nomura, A. Tsuchiya, I. Takahashi, K. Ishikawa, Effects of the carbonate content in carbonate apatite on bone replacement, J. Tissue Eng. Regen. Med. 16 (2022) 200–206, https://doi.org/10.1002/term.3270.
- [57] M.E. Fleet, X. Liu, Accommodation of the carbonate ion in fluorapatite synthesized at high pressure, Am. Mineralog. 93 (2008) 1460–1469, https://doi.org/10.2138/ am.2008.2786.
- [58] A. Bigi, E. Boanini, C. Capuccini, M. Gazzano, Strontium-substituted hydroxyapatite nanocrystals, Inorg. Chim. Acta 360 (2007) 1009–1016, https://doi.org/10.1016/j.ica.2006.07.074.
- [59] L. Bertinetti, C. Drouet, C. Combes, C. Rey, A. Tampieri, S. Coluccia, G. Martra, Surface characteristics of nanocrystalline apatites: effect of Mg surface enrichment on morphology, surface hydration species, and cationic environments, Langmuir 25 (2009) 5647–5654, https://doi.org/10.1021/la804230j.
 [60] C. Drouet, M.T. Carayon, C. Combes, C. Rey, Surface enrichment of biomimetic
- [60] C. Drouet, M.T. Carayon, C. Combes, C. Rey, Surface enrichment of biomimetic apatites with biologically-active ions Mg2+ and Sr2+: a preamble to the activation of bone repair materials, Mater. Sci. Eng. C 28 (2008) 1544–1550, https://doi.org/ 10.1016/j.msec.2008.04.011.
- [61] D. Farlay, G. Panczer, C. Rey, P.D. Delmas, G. Boivin, Mineral maturity and crystallinity index are distinct characteristics of bone mineral, J. Bone Miner. Metab. 28 (2010) 433–445, https://doi.org/10.1007/s00774-009-0146-7.
- [62] R. Astala, M.J. Stott, First principles investigation of mineral component of bone: CO₃ substitutions in hydroxyapatite, Chem. Mater. 17 (2005) 4125–4133, https://doi.org/10.1021/cm050523b
- [63] L.D. Mkukuma, J.M.S. Skakle, I.R. Gibson, C.T. Imrie, R.M. Aspden, D.W.L. Hukins, Effect of the proportion of organic material in bone on thermal decomposition of bone mineral: an investigation of a variety of bones from different species using thermogravimetric analysis coupled to mass spectrometry, high-temperature X-ray diffraction, and Fourier transform infrared spectroscopy, Calcif. Tissue Int. 75 (2004) 321–328, https://doi.org/10.1007/s00223-004-0199-5.
- [64] Y. Sugiura, Y. Saito, T. Endo, Y. Makita, Effect of the ionic radius of alkali metal ions on octacalcium phosphate formation via different substitution modes, Cryst. Growth Des. 19 (2019) 4162–4171, https://doi.org/10.1021/acs.cgd.9b00656.
- [65] Y. Sugiura, Y. Makita, Sodium induces octacalcium phosphate formation and enhances its layer structure by affecting the hydrous layer phosphate, Cryst. Growth Des. 18 (2018) 6165–6171, https://doi.org/10.1021/acs.cgd.8b01030.
- [66] D. Magne, P. Pilet, P. Weiss, G. Daculsi, Fourier transform infrared microspectroscopic investigation of the maturation of nonstoichiometric apatites in mineralized tissues: a horse dentin study, Bone 29 (2001) 547–552, https://doi. org/10.1016/S8756-3282(01)00609-3.
- [67] F. Groot, P. Layrolle, C. Blitterswijk, K. Groot, Biomimetic calcium phosphate coatings on Ti6Al4V: a crystal growth study of octacalcium phosphate and inhibition by Mg²+ and HCO₃, Bone 25 (1999), https://doi.org/10.1016/S8756-3282(99)00145-3.

- [68] C.J.S. Ibsen, D. Chernyshov, H. Birkedal, Apatite formation from amorphous calcium phosphate and mixed amorphous calcium phosphate/amorphous calcium carbonate, Chem. A Eur. J. 22 (2016) 12347–12357, https://doi.org/10.1002/ CHEM 201601280
- [69] C.J.S. Ibsen, H. Leemreize, B.F. Mikladal, J. Skovgaard, M. Bremholm, J. R. Eltzholtz, B.B. Iversen, H. Birkedal, Alkali counterions impact crystallization kinetics of apatite nanocrystals from amorphous calcium phosphate in water at
- high pH, Cryst. Growth Des. 18 (2018) 6723–6728, https://doi.org/10.1021/acs.cgd.8b01008.
- [70] G.H. Nancollas, B. Tomazic, Growth of calcium phosphate on hydroxyapatite crystals. Effect of supersaturation and ionic medium, J. Phys. Chem. 78 (1974) 2218–2225, https://doi.org/10.1021/j100615a007.
- [71] F. Peccati, M. Corno, M. Delle Piane, G. Ulian, P. Ugliengo, G. Valdrè, CO32–mobility in carbonate apatite as revealed by density functional modeling, J. Phys. Chem. C 118 (2013) 1364–1369, https://doi.org/10.1021/JP4108415.